Surface-Structured Bacterial Cellulose with Guided Assembly-Based Biolithography (GAB)

Simone Bottan,[†,∥] Francesco Robotti,[†,∥] Prageeth Jayathissa,[†] Alicia Hegglin,[‡] Nicolas Bahamonde,[†] José A. Heredia-Guerrero,[§] Ilker S. Bayer,[§] Alice Scarpellini,[⊥] Hannes Merker,[‡] Nicole Lindenblatt,[‡] Dimos Poulikakos,[*,†] and Aldo Ferrari[*,†]

[†]Laboratory of Thermodynamics in Emerging Technologies, Department of Mechanical and Process Engineering, ETH Zurich, Sonneggstrasse 3, CH-8092 Zurich, Switzerland, [‡]Division of Plastic Surgery and Hand Surgery, University Hospital Zurich, Raemistrasse 100, 8091 Zurich, Switzerland, [§]Smart Materials, Nanophysics, Istituto Italiano di Tecnologia, Via Morego 30, 16163 Genova, Italy, and [⊥]Nanochemistry, Istituto Italiano di Tecnologia, Via Morego 30, 16163 Genova, Italy. [∥]S.B. and F.R. contributed equally.

ABSTRACT A powerful replica molding methodology to transfer on-demand functional topographies to the surface of bacterial cellulose nanofiber textures is presented. With this method, termed guided assembly-based biolithography (GAB), a surface-structured polydimethylsiloxane (PDMS) mold is introduced at the gas–liquid interface of an *Acetobacter xylinum* culture. Upon bacterial fermentation, the generated bacterial cellulose nanofibers are assembled in a three-dimensional network reproducing the geometric shape imposed by the mold. Additionally, GAB yields directional alignment of individual nanofibers and memory of the transferred geometrical features upon dehydration and rehydration of the substrates. Scanning electron and atomic force microscopy are used to establish the good fidelity of this facile and affordable method. Interaction of surface-structured bacterial cellulose substrates with human fibroblasts and keratinocytes illustrates the efficient control of cellular activities which are fundamental in skin wound healing and tissue regeneration. The deployment of surface-structured bacterial cellulose substrates in model animals as skin wound dressing or body implant further proves the high durability and low inflammatory response to the material over a period of 21 days, demonstrating beneficial effects of surface structure on skin regeneration.

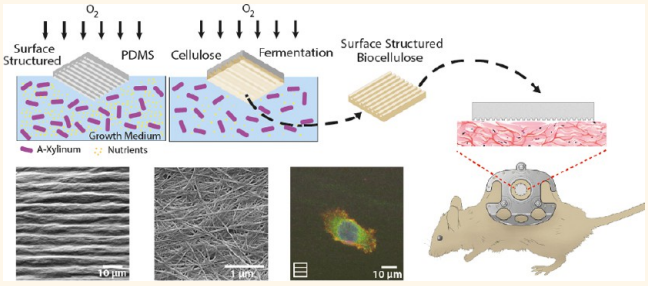

KEYWORDS: bacterial cellulose · topography · contact guidance · fibroblasts · keratinocytes

The performance of artificial materials designed for use in medical applications critically depends on their interaction with the patient tissue and organs.[1,2] Among the constitutive properties that can be specifically tailored, surface topography represents a material-independent physical parameter through which desired responses can be elicited in human cells.[3] Indeed, virtually all tested eukaryotic cell types showed the ability to sense and respond to topographic features in the micron range.[4] The state-of-the-art in the design of microstructured geometries for the interaction with cells is based on regular arrays of periodically repeated topographic features with rationally selected dimensions.[5,6] Most of these substrates are anisotropic and thus provide a directional cue to the adhering cells.[7] In this case, the cell response is expressed by their shape adaptation and by the alignment of migratory patterns with respect to the direction dictated by the topography.[8,9] The ensemble of directional cellular responses related to the substrate topography is defined as contact guidance.[10] Surface-structured biomaterials, which efficiently induce contact guidance, are applied to re-establish or regenerate polarized tissues.[11] These applications include the healing of skin wounds and the population of the luminal surface of cardiovascular implants by endothelial cells.[12,13]

A number of engineering protocols exist for the transfer of topographic patterns to the surface of target biomaterials.[14] In general, the initial pattern design requires the microfabrication of a substrate by means of standard photolithography. The chosen replica-molding process largely depends on

* Address correspondence to aferrari@ethz.ch, dpoulikakos@ethz.ch.

Received for review July 3, 2014 and accepted December 19, 2014.

Published online December 19, 2014
10.1021/nn5036125

the physicochemical properties of the target materials. Thermoplastic polymers are surface-structured by means of nanoimprint lithography (*i.e.*, hot embossing[15]), while elastomers and hydrogels can be shaped by means of soft lithography.[16] A high fidelity negative replica of the original geometry is obtained; however, these procedures require a number of sequential steps.[17] Additionally, the surface structuring of biologically derived polymers has proven to be challenging, owing the peculiar self-assembly properties of these molecules.[18,19]

Cellulose is a well-suited material for body implant applications and has attracted significant research interest due to its durability and the low inflammatory response elicited *in vivo*.[20] The biosynthesis of cellulose takes place not only in plants, but also in bacteria of the *Acetobacteraceae* family.[21] Although identical to cellulose of plant origin in terms of molecular formula, bacterial cellulose is superior in terms purity and degree of polymerization.[22] Bacterial cellulose is generated through the bacterial fermentation of glucose, and the properties of the final substrate can be specifically controlled.[23] These include mechanical resistance,[23] degradability,[24] surface porosity,[25] optical transparency,[26] biochemical functionalization,[27] and three-dimensional shape.[23,28] However, no protocols to transfer desired geometries on the surface of bacterial cellulose exist.

Over the past few years the interest and the commercial use of bacterial cellulose have grown considerably. Applications include products for temporary skin and tissue replacement, for skin wound dressing,[29] and for tissue regeneration.[30] A biocompatibility evaluation of bacterial cellulose was made in Wistar rats by subcutaneous implantation.[20] Up to 12 weeks after implantation no microscopic signs of inflammation, including redness, edema, or exudates around the implanted materials were evident. Additionally, no histological signs of inflammation in the specimen were found. The implanted bacterial cellulose membranes remained intact for at least 90 days.[20,22]

Here we describe a facile and cost-effective method to microstructure the surface of bacterial cellulose. The replica-molding approach, termed guided assembly-based biolithography (GAB), is integrated in the fermentation protocol. GAB yields bacterial cellulose substrates containing the negative replica of a PDMS mold. This structuring was used to transfer topographic features ranging from 1 to 50 μm in the lateral dimension and from 0.2 to 2 μm in the vertical dimension. The resulting geometries are preserved upon cycles of dehydration and rehydration of the bacterial cellulose substrates. GAB-generated topography confers contact guidance properties to the bacterial cellulose substrates upon interaction with human dermal fibroblasts and keratinocytes. The biocompatibility of GAB-structured bacterial cellulose substrates is evaluated in a mouse model. Additionally, the beneficial effect of surface structuring is tested upon skin wound healing *in vivo*. In all, this advancement paves the way toward a new generation of biomaterials coupling the biochemical properties of bacterial cellulose with the interfacing possibilities empowered by the control of surface topography at the micron scale.

RESULTS AND DISCUSSION

Guided Assembly-Based Biolithography (GAB). Surface-structured bacterial cellulose substrates were obtained introducing a PDMS mold at the air-to-liquid interface of a standard *Acetobacter xylinum* fermentation culture (Figure 1). Within 7 days of culture the process reproducibly yielded bacterial cellulose substrates bearing a negative replica of the PDMS topography. Specifically, 15 different PDMS molds were used, featuring gratings (alternating lines of ridges and grooves) with 50% duty cycle, 0.1, 0.6, 0.8, 1, 5, 10, or 50 μm groove depth, and 2, 10, 20, or 100 μm period, respectively (a complete list is provided in Table S1). Additionally, a flat PDMS mold yielding unstructured bacterial cellulose substrates was included as control for the ensuing contact guidance experiments.

The morphologies of the surface-structured bacterial cellulose substrates were investigated using scanning electron microscopy (SEM) and atomic force microscopy (AFM) and compared to the respective PDMS molds. The fidelity of GAB and the edge roughness of the resulting topographical features were evaluated in SEM images of substrates generated using PDMS molds featuring a constant groove depth of 1 μm and increasing lateral period (2, 10, 20, and 100 μm, respectively, Figure 2 and Table S1). A second set of substrates was generated using PDMS molds featuring a constant aspect ratio of 1 and increasing lateral period (10, 20, and 100 μm. Table S1 and Figure S1). The lateral periodicity was transferred with an average deviation from the corresponding mold ranging between 0.5 and 10% (Table 1, Figure 2, Table S2, and Figures S1 and S2). In particular, the lateral periodicity of gratings was transferred with the best fidelity from PDMS molds featuring deeper topographical features (P20−10 and P100−50, Figures S1 and S2). The edge roughness of gratings on bacterial cellulose was significantly higher than in corresponding PDMS molds (Table 1). These results confirm the good fidelity of GAB in transferring geometries with lateral feature size in the range between 1 and 50 μm. Additionally, they indicate that the characteristic fibrous composition of bacterial cellulose hinders the sharpness of topographic feature edges.

Next we analyzed higher magnification SEM images revealing the individual nanofiber density, distribution, and diameter on the surface of bacterial cellulose substrates obtained by GAB (Figure 2 and Figure S8). The average surface porosity (Φ) measured

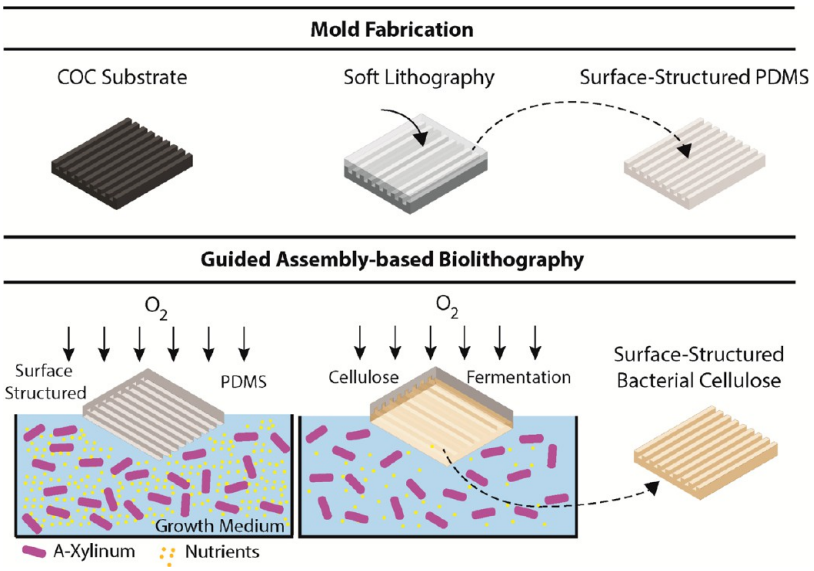

Figure 1. Guided assembly-based biolithography (GAB). An initial mold is generated by hot embossing of a thermoplastic polymer (COC). A negative replica is then obtained on PDMS by a soft-lithography step. Next, the surface-structured PDMS is placed at the interface of the fermentation culture and incubated for up to 7 days. A surface-structured bacterial cellulose substrate is finally produced at the interface and can be easily harvested.

in all surface-structured substrates was higher than the control value (Figure 2 and Figure S1). Thus, the surface structuring of bacterial cellulose yielded a small but consistent decrease of the nanofiber density and diameter. The flat surface of control bacterial cellulose substrates was characterized by a randomly entwined network of fibers with nanometric diameter as previously reported[22] (Figure 2). Interestingly, structured bacterial cellulose substrates showed a visible alignment of individual nanofibers toward the direction of the gratings, which was more evident in the P2−1 sample (Figure 2B). In order to quantify this observation, the overall orientation of individual nanofibers was evaluated in distinct samples (Figure 2 and Figure S1). As expected, the nanofiber directionality was homogeneously distributed in unstructured bacterial cellulose substrates. On the surface of structured bacterial cellulose substrates most nanofibers aligned within 30° to the main direction of the gratings (Figure 2 and Figure S1). Specifically, a significant fraction of nanofibers aligned to P2−1 gratings (22% within 10°, Figure 2B) while the alignment to wider gratings (P10−1 and P20−1, Figure 2C and D) was less efficient (16−17% within 10°). No preferential alignment was detected on very large gratings (P100−1 and P100−50, Figure 2E and Figure S1). The controlled assembly of bacterial cellulose nanofibers can be obtained through the restriction of bacterial motion upon fermentation.[31] The coherent alignment of nanofibers obtained with GAB may similarly depend on the confinement of bacteria along the surface texture on the PDMS mold (Figure 1). To this end, due to the typical size of the bacterial cells,[31] narrow ridges and grooves may harness the motion of individual bacteria more efficiently than corresponding topographical features on larger gratings[31] yielding a better alignment of the nanofibers. Consistently, very large gratings may provide no physical confinement, yielding unbiased nanofiber deposition. Additionally, we tested whether the anisotropic nanofiber alignment resulted in a directional stiffening of the substrates. Mechanical tests (Figure S3) confirmed the symmetric mechanical behavior of control flat substrates. Directional stiffening was measured along the direction parallel to the gratings (as compared to the direction perpendicular to it) on the P10−1 sample (Figure S3A). This finding suggests that the alignment of nanofibers may extend to deeper regions thus influencing the bulk mechanical properties of the substrate (Figure S3B−D). In summary, these data demonstrate that topographies with lateral feature size in the range between 1 and 50 μm are reliably transferred on bacterial cellulose by means of GAB and that the process involves the alignment of individual cellulose nanofibers.

The vertical size of gratings transferred on bacterial cellulose by GAB was evaluated using AFM imaging (Figure 3). The corresponding depth profiles showed that gratings were generally shallower than the corresponding PDMS molds (Figure S2). For substrates generated on molds featuring 1 μm deep grooves (P2−1, P10−1, P20−1 and P100−1) the groove depth ranged from 0.2 to 0.5 μm (on substrates P2−1 and P10−1, respectively; Figure 3J) and reached 1 μm only on large gratings (P100−1). Deeper gratings could be obtained using PDMS molds with constant aspect ratio and increasing lateral periodicity (Figure 3K). The shallowest PDMS mold that could be transferred on bacterial cellulose featured gratings with groove depth of

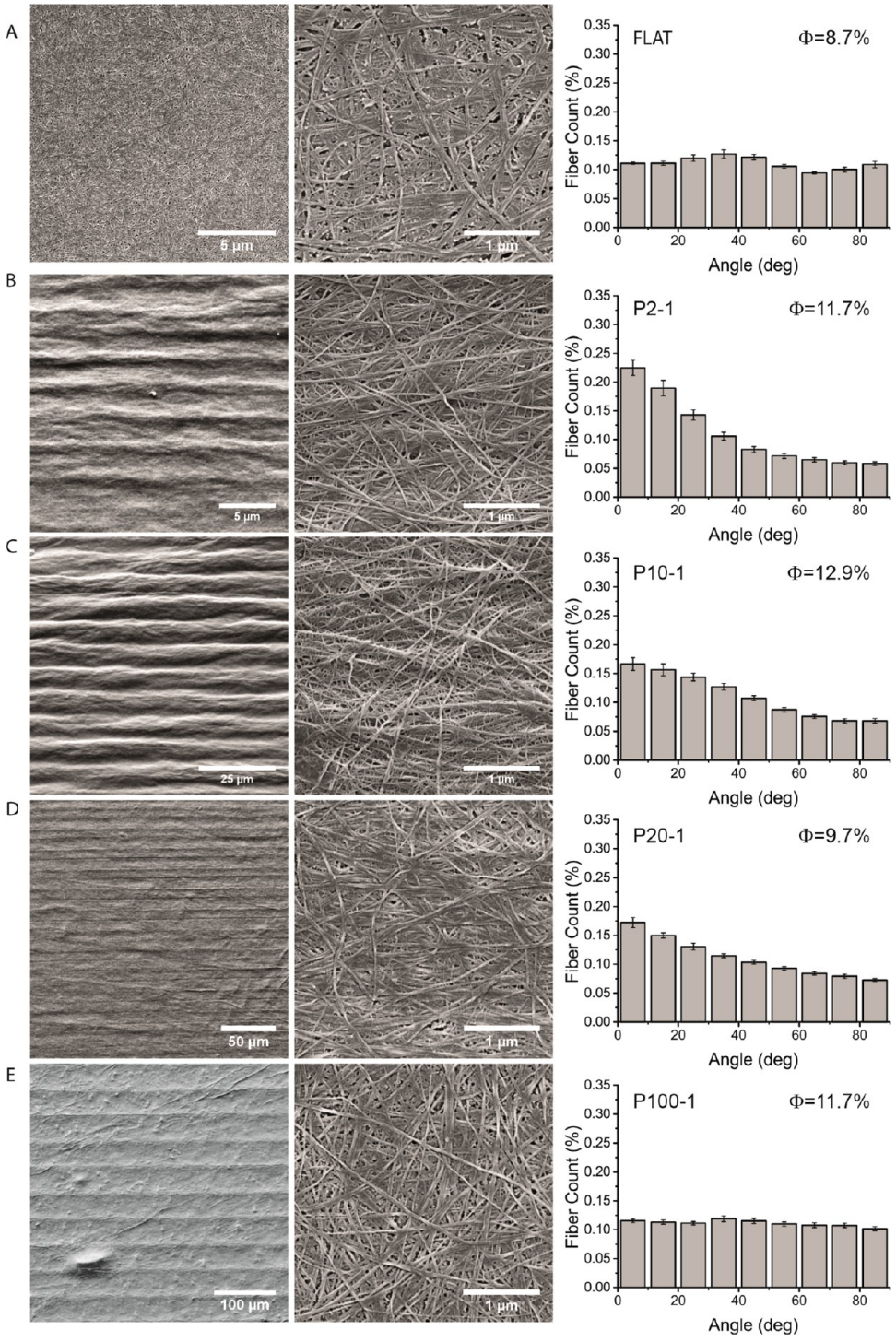

Figure 2. Lateral characterization of surface-structured bacterial cellulose. Representative scanning electron microscopy (SEM) of control flat (FLAT) bacterial cellulose substrates or gratings generated using PDMS molds featuring constant groove depth of 1 μm, 50% duty cycle and increasing lateral period of 2, 10, 20, and 100 μm, respectively (left column). Corresponding zoomed views of the substrates showing individual cellulose nanofibers (middle column), and the quantification of the nanofibers orientation (right column). The histograms report the distribution of individual nanofiber alignment where 0° corresponds to the main direction of the gratings. Error bars correspond to the standard error of the mean. Values of surface porosity (Φ) of the nanofibers network are reported in the upper right corner of each graph.

0.6 μm (Table S1 and Figures S1 and S2). Shallower molds (Table S1 and Figure S1) yielded no visible surface structure on bacterial cellulose (Figure S1). Additionally, the phase image analysis (Figure S9) shows no difference in the mechanical response of ridges and grooves indicating an homogeneous stiffness of the substrates. In summary, geometries with vertical feature size between 0.2 and 2 μm and aspect ratio

TABLE 1. Lateral Fidelity of Guided Assembly-Based Biolithography (GAB)[a]

sample	period (μm)	lateral replica fidelity (%)	edge roughness (nm)
P2−1	2.1 ± 0.1	9.0	186 ± 40
P10−1	10.0 ± 0.2	2.8	390 ± 75
P20−1	21.4 ± 0.1	8.6	368 ± 92
P100−1	99.2 ± 0.5	1.6	595 ± 130
P10−5	10.6 ± 0.1	9.9	206 ± 15
P20−10	20.3 ± 0.1	0.8	255 ± 26
P100−50	100.1 ± 0.3	0.4	452 ± 44

[a] Values of lateral periodicity, replica fidelity and edge roughness measured from SEM images of surface-structured bacterial cellulose substrates generated using PDMS molds featuring constant groove depth of 1 μm (P2−1, P10−1, P20−1 and P100−1) or a constant aspect ratio of 1 (P10−5, P20−10, and P100−50), 50% duty cycle and increasing lateral period of 2, 10, 20, and 100 μm, respectively. The measurements are reported as average values ± the standard error of the mean.

between 0.02 and 0.2 could be generated on bacterial cellulose by means of GAB.

Importantly, both the lateral and the vertical feature size of gratings did not vary significantly upon dehydration and rehydration of the surface-structured bacterial cellulose substrates (Figure S4). Therefore, despite the significant overall weight loss induced by the process of dehydration and rehydration (~90%, Figure S4), bacterial cellulose substrates displayed a full memory of the topography introduced by GAB.

Contact Guidance Efficiency of Surface-Structured Bacterial Cellulose. The efficiency of surface-structured bacterial cellulose substrates in inducing oriented cellular activities was tested using freshly isolated human dermal fibroblasts (HDF) and human keratinocytes (HaCaT). Specifically, geometries obtained using molds featuring a groove depth of 0.8 μm, and a lateral period of 2 or 10 μm (hereafter denoted as P2 and P10, respectively. Table S1) were selected, since their contact guidance efficiency is well established.[10,12] HDF and HaCaT cells were selected for two reasons: first, for their critical contribution to skin wound healing *in vivo*.[12] Second, for their well-established ability in reading and responding to the surface topography of biomaterials.[8] The contact guidance efficiency was expressed by two cellular responses to the anisotropic topographies: the cell shape and orientation and the alignment of migratory pathways to the direction dictated by the gratings.

To favor the cell interaction, the bacterial cellulose substrates were coated with gelatin and cells were let to adhere for 12 h. It is worth noting that the coating procedure of cellulose substrates preserved both the micron-scale geometry introduced and the corresponding alignment of cellulose nanofibers on the surface (Figure S5). On these substrates the cell density, area, and elongation were measured, showing both the cell cytoskeleton and the adhesion by means of immunostaining (Figures 4 and 5). HaCaT cells did not adhere well to unstructured bacterial cellulose

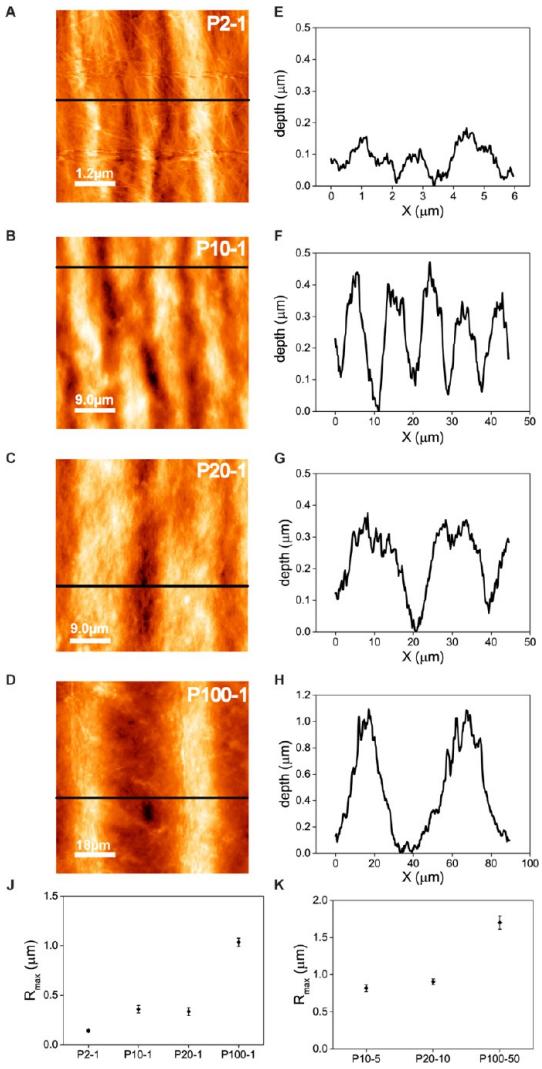

Figure 3. Vertical characterization of surface-structured bacterial cellulose. (A−D) Representative atomic force micrographs of surface-structured bacterial cellulose substrates featuring gratings (left column) and (E−H) corresponding depth profiles (right column). All gratings were generated using PDMS molds with a constant groove depth of 1 μm, 50% duty cycle and an increasing lateral period of 2 (P2−1), 10 (P10−1), 20 (P20−1) and 100 (P20−1) μm (A), (B), (C) and (D), respectively. Profile depths (R_{max}) for gratings generated using PDMS molds with constant (J) groove depth or (K) aspect ratio. Error bars correspond to the standard error of the mean.

substrates and remained circular without forming evident cell-to-substrate adhesions or actin filaments (Figure 4). Similarly, only a partial adhesion and spreading were detected on gratings with few small cell-to-substrate adhesions and a poorly structured actin cytoskeleton (Figure 4B and C). Therefore, the surface topography had a limited effect on the adhesion and spreading of these cells (Figure 4D and E). HDF adhered well to gelatin-coated bacterial cellulose demonstrating full spreading and a well-defined polarization as reflected by the measurement of the cell elongation (Figure 4D) and cell area (Figure 4F). Because of the better adhesion shown by HDF the analysis of contact

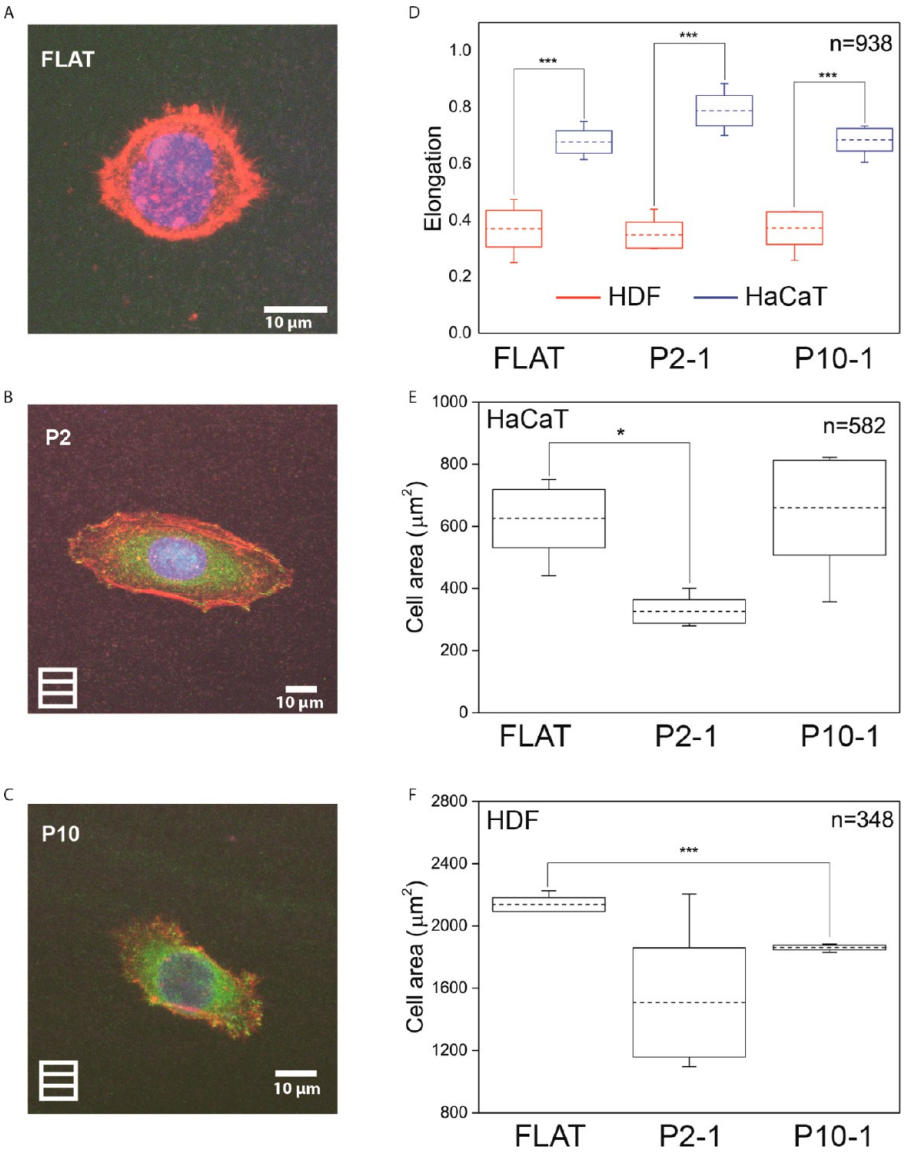

Figure 4. Cell spreading on surface-structured bacterial cellulose. (A−C) Representative confocal images of immunofluorescent staining revealing the distribution of filamentous actin (red) and vinculin (green) in human keratinocytes (HaCaT) adhering to bacterial cellulose substrates featuring an unstructured control surface (FLAT), or gratings (P2 or P10). The orientation of gratings is reported in the lower left corner. (D−F) Quantification of cell spreading. The box plots report the mean values for cell elongation and cell area measured in HDF and/or HaCaT adhering to flat substrates or gratings. The population mean is reported as a horizontal dashed line in a rectangular box whose vertical length represents the standard error of the mean. Whiskers individuate the 5 and 95 percentiles. The total number of counted cells is reported in the left corner of each graph. Significant differences between the population means are indicated by asterisks (* for $p < 0.05$ and * for $p < 0.001$).**

guidance efficiency on surface-structured bacterial cellulose substrates was focused on this cells type. On all bacterial cellulose substrates HDF were characterized by evident actin stress fibers and mature cell-to-substrate adhesions (Figure 5A). Interestingly, a higher cell density was measured on gratings as compared to control flat substrates (Figure 5B). This effect may be mediated by the presence of grooves channeling cell adhesion in the early phases of spreading.[9]

On unstructured bacterial cellulose, HDF polarized randomly and no preferential direction of alignment was measured (Figure 5C). Remarkably, a specific cell alignment was detected on structured bacterial cellulose substrates (Figure 5C). In particular, the majority of measured cells aligned within 30° to the direction of gratings (Figure 5D). Interestingly, a significant fraction of cells aligned at a 20° angle with the direction dictated by topography (Figure 5D). Two hypotheses can explain the measured distribution of cell orientation. We have previously reported that anisotropic surface topographies interfere with the establishment and maturation of cell-to-substrate adhesions.[11] The resulting confinement of adhesions on ridges produces a polarization of the actin cytoskeleton and overall forces the cell to realign along the direction dictated by the topography.[11,7] However, in

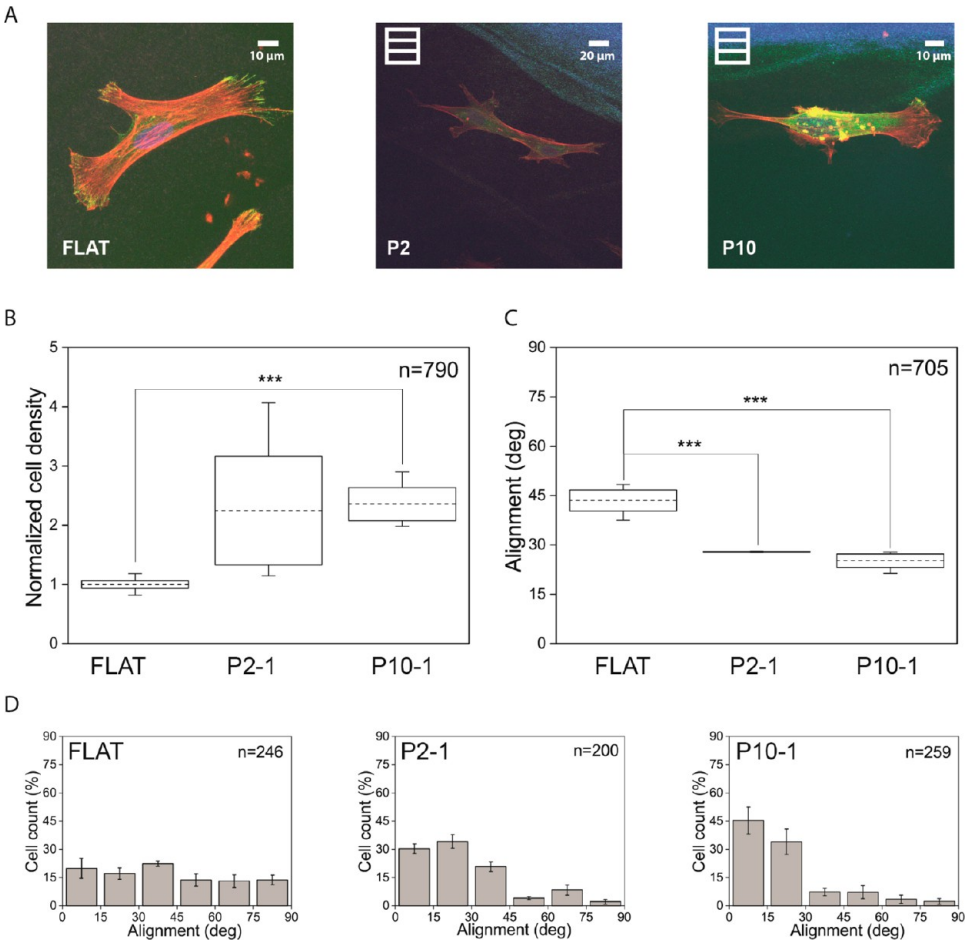

Figure 5. HDF polarization on surface-structured bacterial cellulose. (A) Representative confocal images of immunofluorescent staining revealing the distribution of filamentous actin (red) and vinculin (green) in human dermal fibroblasts (HDF) adhering to bacterial cellulose substrates featuring an unstructured control surface (FLAT), or gratings (P2 or P10). The orientation of gratings is reported in the upper left corner. (B) Quantification of HDF cell density on the tested substrates. (C) Quantification of cell alignment to the surface structures. The population means are reported as a horizontal dashed line in a rectangular box whose vertical length represents the standard error of the mean. Whiskers individuate the 5 and 95 percentiles. Significant differences between the population means are indicated by asterisks (for $p < 0.01$ and *** for $p < 0.001$). (D) Corresponding histograms reporting the cell alignment distribution. Error bars correspond to the standard error of the mean. The total number of counted cells is reported in the right corner of each graph.**

this scenario narrow ridges and grooves should more efficiently interfere with the maturation of cell-to-substrate adhesions established by HDF on bacterial cellulose, yielding a strict coalignment of the cell cytoskeleton. An alternative explanation considers the peculiar orientation of individual nanofibers on the surface of structured bacterial cellulose (Figure 2 and Figure S5). Cells interacting with gratings are therefore exposed to multiple overlapping topographic and mechanical signals generated by the gratings and by the cellulose nanofibers (Figure 2). The interaction with nano- or microscale topographic features is mediated by different cell machineries.[7,32] This may result in conflicting guidance signals read by cells and yielding a range of intermediate cell alignments.

The displacement of HDF was captured by long (6 h or more) time-lapses of fluorescently labeled cells, enabling the determination of the migratory paths of cells interacting with bacterial cellulose substrates (Figure 6 and Videos S1 and S2). The analysis of individual tracks provided information on cell migration alignment (Figure 6A), velocity and straightness. The velocity of HDF migrating on unstructured cellulose substrates was of 19.5 $\pm$ 0.3 μm/h similar to what reported for fibroblasts interacting with other biomaterials.[33] Interestingly, the velocity of migration was significantly reduced in cells interacting with structured bacterial cellulose substrates (16.1 $\pm$ 0.4 and 12.8 $\pm$ 0.4 μm/h on gratings P2 and P10, respectively; Figure S6). The track directionality exhibited an opposite trend with more directed tracks on gratings P10 (straightness of 0.73 $\pm$ 0.01) than on gratings P2 or flat substrates (0.66 $\pm$ 0.01 and 0.67 $\pm$ 0.01, respectively; Figure S6). Additionally, HDF moved along randomly aligned tracks on flat bacterial cellulose substrates (Figure 6B), while the interaction with topography efficiently confined migration along the direction

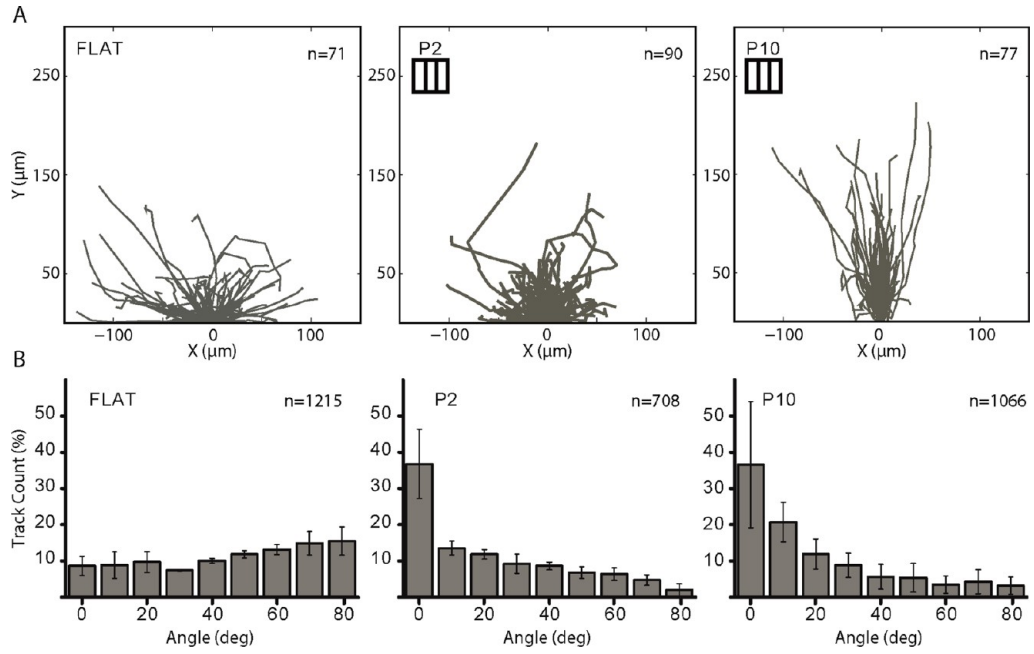

Figure 6. Cell migration on surface-structured bacterial cellulose. (A) Tracks extracted from time-lapses of HDF migrating on FLAT bacterial cellulose substrates or gratings (P2 or P10). The orientation of gratings is reported in the upper left corner. The total number of tracks is reported in the upper right corner of each panel. (B) The histograms report the corresponding distribution of individual cell tracks. Error bars correspond to the standard error of the mean.

dictated by gratings. Alignment of migration was more evident on P10 substrates with more than 70% of analyzed tracks oriented within 20° to the direction of gratings (Figure 6B).

In all, these data demonstrate that anisotropic topographies transferred on bacterial cellulose substrates by means of GAB were efficient in inducing migration alignment with a more prominent effect on gratings with feature size comparable to the cell body. The reduction in migration velocity detected on structured substrates has already been reported for other cell types.[34] For cells growing in confluent monolayers this effect has been linked to the strengthening of cell-to-cell junctions and the resulting switch to collective migration. Fibroblast do not form connected monolayers and migrate following individual migratory pathways. However, the confinement induced by gratings is bidirectional, and may produce phases of stall or of changes in directionality resulting in an overall reduced cell displacement.

Biocompatibility of Surface-Structured Bacterial Cellulose. To evaluate the biocompatibility and measure the inflammatory response elicited *in vivo*, the bacterial cellulose substrates were applied as dressing on artificial wounds created in the mouse modified dorsal skin chamber (MDSC) set up[35] (Figure S7). Additionally, a second replica of the substrates was implanted in a skin pocket located in the groin of the same animal (Figure 7). In total, three groups of 6 animals each received bacterial cellulose substrates (FLAT, P2 or P10, respectively). An additional group of mice received a full thickness homologous skin graft in the MDSC. This group was included as control yielding minimal inflammatory response and optimal wound healing.[35]

The influence of structured and unstructured bacterial cellulose substrates on vascularization of the artificial wound bed in the MDSC was quantified by intravital microscopy (IVM). Here, standard angiogenic parameters (*i.e.*, the diameter and the length of capillaries) were analyzed over a period of 21 days (Figure 7A and B). The results reported in Figure 7 show that in none of the animals receiving bacterial cellulose a significant difference in the length or diameter of capillaries could be detected (Figure 7A and B). Additionally, the dynamics and extent of the angiogenic response at the interface with the bacterial cellulose substrates were comparable to that measured in the control group receiving full-thickness skin grafts. In particular, in all groups the average diameter of capillaries linearly increased in the first 3 to 5 days after wounding up to a maximum value ranging between 10.4 ± 0.5 μm and 10.9 ± 0.6 μm (in the FLAT and control groups, respectively). This peak was temporary and the capillaries shrank stably to the original diameter by day 10 (Figure 7A). The length of capillaries displayed minimal variations over the tested period (Figure 7B) with an overall tendency to decrease within the first 5 days after wounding and a recovery to basal levels in the following 10 days.

The histological assessment of substrates deployed in the DSC or in the skin pocket provided evidence that the structure of all bacterial cellulose substrates was fully preserved (Figure 7C) and that no cellular ingrowth was detectable (Figure 7C). These data confirm

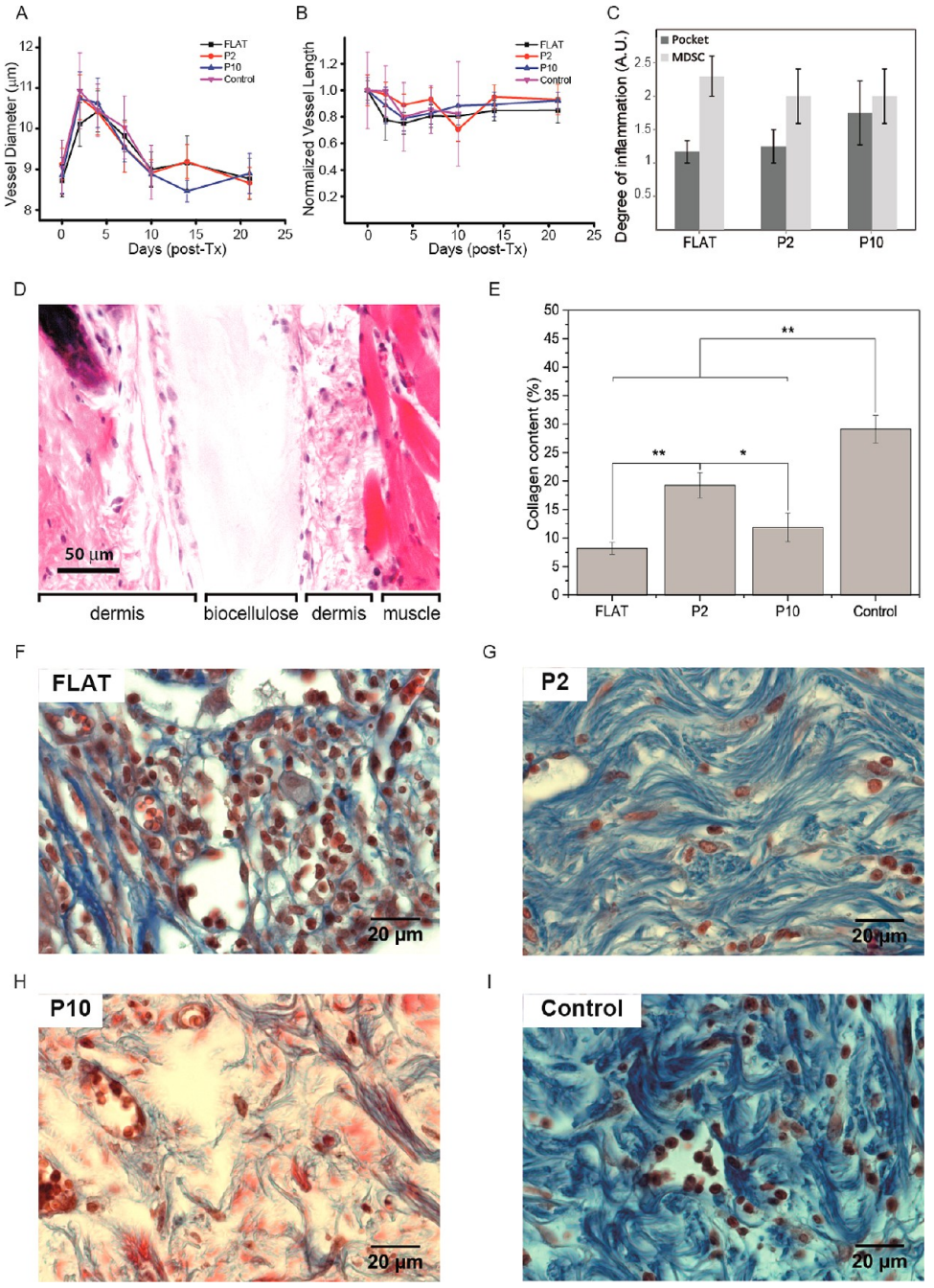

Figure 7. Animal tests with surface-structured bacterial cellulose. (A) Dynamics of average blood vessel diameter at the wound created in the dorsal skin chamber (MDSC) setup. The vessel diameter was measured from images acquired through intravital microscopy at each day of measure for a total of 21 days. Animals received either unstructured bacterial cellulose substrates (FLAT) or substrates structured with gratings (P2 or P10, respectively). Control animals received a homologous skin graft as wound dressing. (B) Corresponding dynamics of average vessel length. (C) Histological slice of a bacterial cellulose substrate implanted in a skin pocket. (D) Comparison of degree of inflammation at the MDSC and in the skin pocket of animals receiving bacterial cellulose substrates. The error bars correspond to the standard error of the mean. (E) Quantification of collagen content in the wound bed at 21 days after wounding. The histograms report the wound surface fraction that contains newly deposited collagen. Error bars correspond to the standard error of the mean. Significant differences between the population means are indicated by asterisks (* for $p < 0.05$, ** for $p < 0.01$). (F–I) Representative histological images of collagen formation revealing collagen fibers (blue) and fibroblast infiltration (dark/brown nuclei) in the wound bed for each of the tested conditions (Flat, P2, P10 and Control in F, G, H, and I, respectively).

that bacterial cellulose was not degraded over a period of 21 days and that no tissue integration or fibrotic encapsulation was visible. The presence of inflammatory cells around the substrates was determined by the PAN-inflammatory marker coronin 1[36] (Figure 7C). Animals receiving unstructured bacterial cellulose displayed a higher number of inflammatory cells at the interface with the substrate deployed in the MDSC as

compared to the one in the skin pocket (Figure 7D). Such difference was not detected in animals receiving surface-structured bacterial cellulose substrates, which displayed a comparable population of inflammatory cells at the two sites. This corresponded to a reduced inflammation at the interface with the MDSC substrate (Figure 7D). These data suggest that the dynamics and extent of the inflammatory process elicited by bacterial cellulose substrates as full implants (skin pocket) or as wound dressing (MDSC) was minimal with a beneficial effect enabled by the presence of a surface structure. This result is in line with other reports indicating that rough biomaterials may be less inflammatory than identical ones fabricated into a smooth, solid form.[37] However, further studies are needed to identify the responsible biological mechanisms.

The generation of a newly deposited collagen matrix upon wound healing expresses the efficiency of fibroblast migration into the wound site and represents a positive prognostic indicator for tissue regeneration.[38] The histological collagen formation and distribution analysis (Figure 7) of the wound beds suggests that the surface-structured bacterial cellulose substrates were able to promote fibroblast migration, collagen deposition and wound closure more efficiently than the unstructured, FLAT counterparts. In particular, by day 21 after wounding, the group of animals that received surface-structured bacterial cellulose featuring 2 μm periodic gratings (P2) was able to re-establish a dense, homogeneously distributed layer of collagen fibers (Figure 7G). Additionally, the wound bed was devoid of any sign of inflammation and characterized by the abundant presence of fibroblasts. The group of animals that received 10 μm gratings (P10) also showed collagen fiber formation and presence of fibroblasts in the wound bed (Figure 7H). However, the extent of newly formed collagen was significantly different in the two conditions, with a 60% higher collagen content in the P2 case (Figure 7E). Importantly, the corresponding wound area in animals that received unstructured bacterial cellulose (FLAT) displayed a granulation tissue featuring only few developed and organized collagen fibers (Figure 7I). As expected, the control group of animals receiving a full-thickness homologous skin graft showed the most efficient collagen deposition (Figure 7I). These data indicate that a faster and more complete healing of the wounded area was obtained in animals treated with P2 substrates as compared to a delayed and incomplete healing of wounds treated with unstructured bacterial cellulose. In all, these results provide a first indication that the presence of a specific surface topography can significantly improve the regeneration of a functional tissue upon skin wound healing *in vivo*.

CONCLUSIONS

We introduced and demonstrated guided assembly-based biolithography (GAB), a powerful process to transfer on demand geometries (textures) on the surface of bacterial cellulose substrates. The approach is based on standard bacterial fermentation of glucose into bacterial cellulose, confined at the interface of a soft-lithographic PDMS mold. This replica-molding process successfully generated topographies in the range between 1 to 50 μm lateral feature size and 0.2 to 2 μm vertical feature size on the surface of bacterial cellulose substrates. The surface topography was stable upon dehydration and rehydration of the substrates and was linked to a corresponding alignment of the cellulose nanofibers. The interaction with human cells involved in the process of skin wound healing demonstrated that anisotropic topographies transferred on bacterial cellulose by GAB are effective in inducing contact guidance and therefore orient both the cell polarization and the migratory patterns. The animal tests indicate this new biomaterial to be durable and to have beneficial effects on tissue regeneration upon skin wound healing. When introduced as wound dressing or implant in animal models the structured bacterial cellulose substrates were not degraded and not invaded by the host cells over a period of 21 days. Additionally, the levels of vascularization and inflammation were comparable to those elicited at the interface with an autologous full skin graft. Fibroblast infiltration and new collagen deposition in the wound bed were promoted by the surface structures as compared to the flat substrates. In all, the developed method makes possible the generation of novel, textured biomaterials, coupling the desirable biochemical properties of bacterial cellulose to the interfacing possibilities stemming from the rational control of surface topography.

MATERIALS AND METHODS

Bacterial Cellulose Fermentation. Microstructured molds for GAB were made of polydimethylsiloxane (PDMS, Dow Corning, USA) at a 1:10 mixing ratio (Figure 1) and fabricated through standard soft lithography.[39] Briefly, the mixed PDMS was degassed in a vacuum chamber for 10 min to remove trapped air and immediately poured onto untreated cyclic olefin copolymer (COC) substrates containing gratings. COC substrates were previously imprinted using nanoimprint lithography as reported.[9,13] In particular, several types of COC gratings were used, which featured line width and pitch of alternatively 1, 5, 10, or 50 μm. The groove depth was 0.1, 0.6, or 1 μm. For selected periods additional groove depths of 0.8, 5, 10, and 50 μm were tested (Table S1). After pouring on the COC molds, the PDMS was briefly degassed for a second time and cured for 4 h at 60 °C.[12] The cured PDMS patches were then carefully separated from the COC mold using tweezers. Control flat patches were similarly created by pouring PDMS on flat COC substrates.

Wild type *Acetobacter xylinum* strain ATCC-700178 (LGC Standards, Wesel, Germany) was used for bacterial cellulose fermentation. The bacteria were grown in a medium prepared as reported in Table S3[40] and sterilized by autoclaving. In order to generate surface-structured bacterial cellulose substrates, 5 mL of medium were distributed in standard 6-well-plates. PDMS molds were then placed in each well, with surface topography in contact with the medium. Bacterial cultures were incubated at 26.5 °C in saturated humidity and steady environments for 7 days. At the end of the culturing period a thick (3 to 4 mm) cellulose layer was formed at the interface with the PDMS molds. Bacterial cellulose substrates were then harvested after removing the PDMS molds. To remove bacteria from the bacterial cellulose the patches were washed in NaOH 1 M for 80 min at 80 °C, and subsequently in deionized (DI) water at RT until neutral pH was reestablished. The bacterial cellulose substrates were fully hydrated upon harvesting from the bacterial fermentation culture. This stage is defined as nondehydrated bacterial cellulose (NDH, Figure S4). The NDH substrates were then washed and dehydrated overnight at room temperature. Dehydrated cellulose substrates (DH) were then rehydrated with DI water. Finally, the rehydrated substrates (RH) were autoclaved (121 °C, 1.1 bar for 15 min) and stored in PBS at 4 °C. Unless otherwise specified all reported experiments were performed using RH substrates.

Characterization of Bacterial Cellulose. After preparation, the surface-structured bacterial cellulose substrates were characterized using scanning electron microscope (SEM) and atomic force microscope (AFM) imaging. To prepare the samples for SEM, the substrates were washed twice in Milli-Q water, and then rinsed for 10 min in increasing concentrations of filtered ethanol (30, 50, 70, 90 and 95%). They were then rinsed twice in 100% ethanol for 15 min each. Ethanol dehydration was followed by gradual replacement with hexamethyldisilazane (Sigma-Aldrich) that was let to evaporate in a fume hood overnight. Samples were finally coated with a 5 nm-thick film of gold/palladium (60/40 wt %). The substrates were imaged using a JEOL JSM-7500FA scanning electron microscope (SEM), equipped with a cold field emission gun (FEG). Initially, low magnification images at 30° tilt angle were acquired, to allow for perspective 3D imaging of surface topography. The bacterial cellulose nanofibers were imaged at higher magnification and resolution, operating the machine at an acceleration voltage 2 kV in order to minimize any possible beam damage effect. In both cases the SEM imaging was performed by collecting secondary electron (SE) signal.

Atomic force microscopy (AFM) analysis was performed using a XE-100 psia instrument (Park Systems) and a Nanowizard III (JPK Instruments, Germany) mounted on an Axio Observer D1 (Carl Zeiss, Germany) inverted optical microscope. The images were acquired in noncontact mode, in the regime of attractive forces, working in air in a vibration-insulated environment (Table Stable TS-150). Single beam silicon cantilevers coated with aluminum on the reflective side (type PPP-NCHR-10, Nanosensors) with typical elastic constant of 42 N m^{-1} and nominal tip radii of less than 10 nm were used with a drive frequency of ~295 kHz. Measurements were taken at a scan rate of 0.2 Hz and different zooms, depending on the topography of zoom. To ensure the reproducibility of the measurements at least six well separated areas of each sample were inspected. The images presented reflect representative topographic patterns (Figures 2 and 3).

Mechanical Tests. The mechanical properties of the bacterial cellulose substrates were determined by uniaxial tensile tests (Figure S3) as reported in Röhrnbauer and Mazza.[41] Briefly, the samples were analyzed in the parallel or perpendicular directions with respect to the fiber orientation. The dimension of the samples was 10 × 10 mm. The tensile tests were performed using a custom-built tension setup. It consisted of a tensile test machine with two hydraulic actuators (242 Actuator, MTS Systems Corp., Eden Praire, MN, USA), each with 2.7 kN capacity, mounted horizontally on a steel plate. 100 N load cells (SMT S-Type, Interface Inc., Scottsdale, AZ, USA) were applied for force measurements. For the uniaxial stress tests, specific calibration files for the range up to 20 N, providing higher resolution in the low force range, were used. Custom-made clamps equipped with sandpaper at the clamping faces were directly attached to the load cells. The samples were mounted in two parallel clamps with an initial chuck width of 3 mm. Monotonic strain to failure tests were performed under displacement controlled conditions, with a displacement rate of 0.04 mm/s, which corresponds to an elongation rate of 0.38% nominal strain per second. The force–displacement data were sampled with a frequency of 100 Hz.

Mammalian Cell Cultures. Human dermal foreskin fibroblasts (HDF) were supplied by the Tissue Biology Research Unit (Department of Surgery, University Children's Hospital Zurich, CH) and obtained according to the principles of the Declaration of Helsinki. Briefly, juvenile foreskin samples were digested overnight at 4 °C in Dispase (0.5 mg mL^{-1}, Roche, CH) in Hank's buffered salt solution (HBSS without Ca^{2+} and Mg^{2+}, Invitrogen) containing 5 mg mL^{-1} gentamycin. This allowed subsequent separation of epidermis and dermis using forceps. To establish primary HDF cultures, the dermis was dissociated into single-cell suspensions using HBSS containing collagenase III (1 mg mL^{-1}, Worthington Biochem., USA) and Dispase (0.5 mg mL^{-1}, Roche) at 37 °C for 1 h. Finally, the cells were cultured in RPMI-1640 medium supplemented with 10% v/v fetal bovine serum (FBS), 2 mML-glutamine, 100 U mL^{-1} penicillin and 100 mg mL^{-1} streptomycin (all from Sigma-Aldrich) and maintained at 37 °C and 5% CO_2. Human keratinocyte (HaCaT[42]) were a gift of Prof. Sabine Werner (ETH Zurich). The cells were cultured DMEM supplemented with 10% v/v FBS 2 mML-glutamine, 100U mL^{-1} penicillin and 100 mg mL^{-1} streptomycin (all from Sigma) and maintained at 37 °C and 5% CO_2. In all reported experiments, cells with less than six passages *in vitro* were used.

Noncoated, pristine bacterial cellulose substrates were not suitable for cell adhesion and growth, therefore to assess contact guidance, sterile bacterial cellulose substrates were coated with gelatin before cell seeding. Gelatin coating was performed as previously reported.[13] Briefly, 1.5% gelatin (Merck, USA) in water was initially added to the samples and left to adsorb for 1 h at RT. Subsequently, the gelatin was cross-linked by incubating with 2% glutaraldehyde (Sigma) in water for 15 min at RT. After a sterilization step with 70% ethanol in PBS (Sigma), the substrates were washed 5 times in PBS (5 min each) and then left overnight at RT in 2 mM glycine (Sigma) in PBS to neutralize the glutaraldehyde. Finally, the bacterial cellulose substrates were washed 5 times in PBS and stored at 4 °C until use.

For cell polarization experiments (Figures 4 and 5) nonconfluent cells were trypsinized and seeded on the bacterial cellulose substrates at final density between 1 and 3.5 × 10^4 cells/cm^{-2}. Cells were incubated for 12 h before fixation and imaging. For the cell migration experiments, HDF were treated for 30 min with 5-chloromethylfluorescein diacetate (CellTracker Green CMFDA, Invitrogen) at a final concentration of 1.5 mg mL^{-1} and then trypsinized and seeded on the bacterial cellulose substrates. Samples were incubated for 12 h and then immediately imaged.

Immunostaining. To visualize the focal adhesions established by cells on the bacterial cellulose substrates the following primary antibody was used: mouse antivinculin (V4505) from Sigma. The secondary antibody was a donkey antimouse-alexa-488 (A-21202) from Invitrogen. Filamentous actin was visualized using TRITC-phalloidin (Sigma).

Cells were fixed and permeabilized for 10 min with 3% paraformaldehyde (PFA) and 0.5% Triton-X100 in PBS at room temperature (RT). The cells were then postfixed with 3% PFA in PBS for 15 min. After washing the samples three times for 5 min with PBS, they were incubated with 5% bovine serum albumin (BSA) in PBS for 1 h at RT. The samples were incubated with TRITC-phalloidin (Sigma, USA) and with mouse antivinculin primary antibody overnight at 4 °C.

Subsequently, the samples were rinsed four times for 1 h with 5% BSA in PBS and then incubated with donkey anti-mouse-alexa-488 secondary antibody for 45 min at RT. Finally, the samples were washed three times (1 h each) in PBS, postfixed for 2 min in 3% PFA, briefly washed again with PBS, mounted with DAPI-containing Vectashield (Vector Laboratories Inc., USA) and immediately imaged.

Wide-Field Microscopy. Wide-field imaging was performed with a 4X, 0.45 NA long-distance objective (Plan Fluor, Nikon)

using an inverted Nikon-Ti wide-field microscope (Nikon, Japan) equipped with an Orca R-2 CCD camera (Hamamatsu Photonics, Japan). After patch mounting, the plates were placed under the microscope in an incubated chamber (Life Imaging Services, CH), where temperature, CO_2 concentration, and humidity were maintained at 37 °C, 5%, and 95% respectively. Movies of migrating HDF were acquired with a time resolution of 30 min for a total of 6 h or more. At each time of measurement, a transmission and a fluorescent image were acquired using a differential interference contrast (DIC) and a FITC filter set, respectively.

Confocal images of cells interacting with bacterial cellulose substrates were collected with a Leica SP2-FCS (Leica, Germany) using a 63X, 1.4 NA, oil immersion objective (Plan-Apo, Leica). Emission from DAPI was excited with the 405 nm wavelength of a Solid State laser and collected in the 450−480 nm optical window. The Alexa488 emission was excited with the 488 nm wavelength of a HeNe laser and collected in the 500−540 nm optical window. Finally, the TRITC emission was excited with the 555 nm wavelength of a HeNe laser and collected in the 600−800 nm optical window. For each sample 15 Z-stacks of individual cells were imaged, collecting three-channels with lateral resolution of 116 nm/px and vertical resolution of 300 nm/px.

Animal Experiments. All experiments were carried out in accordance with the Swiss legislation for the protection of animals and the National Institutes of Health Guide for the Care and Use of Laboratory Animals (Institute of Laboratory Animal Resources, National Research Council). Male C57BL/6J mice with a body weight of 25 to 35 g ($n = 18$) were purchased from LTK Laboratories, Fuellingsdorf, Switzerland. Animals were housed in individual cages with a 12 h light/dark cycle and given water and food ad libitum and treated humanely.

To study the revascularization process the modified dorsal skin fold chamber (MDSC) was used as described by Lindenblatt *et al.*[35] Briefly, for chamber implantation, two symmetrical titanium frames were mounted on a dorsal skin fold of the animal (Figure S7). One skin layer was then completely removed in a circular area of 15 mm in diameter, and the remaining layers (consisting of striated skin muscle, subcutaneous tissue and skin) were covered with a glass coverslip incorporated into one of the titanium frames. Before skin grafting, a recovery period of 3 days was allowed. Then, skin and most parts of the hypodermal fat layer were carefully removed in a circular area of 7 mm in diameter from the back of the chamber in order to create an artificial full-thickness wound. The defect on the back of the chamber was then covered with bacterial cellulose substrates (FLAT, P2 and P10) and covered with a glass coverslip incorporated into the other titanium frame. Surface-structured bacterial cellulose substrates were placed with gratings directed toward the wound bed. Additionally, to investigate the biocompatibility of bacterial cellulose substrates, all animals received a replica of the same bacterial cellulose substrate in a skin pocket in the groin.

Intravital Microscopy. Intravital microscopy was carried at 0, 2, 4, 7, 10, 14, and 21 days post-Tx. Microscopic images were taken at 8 different areas within the center and periphery of the wound bed underlying the implanted bacterial cellulose substrates.

After injection of 0.15 mL of fluorescein isothiocyanate (FITC)−labeled dextran (1%; molecular weight 70 000; Sigma-Aldrich, Munich, Germany) into the tail vein, the microcirculation at the wound bed and the bacterial cellulose substrate was visualized by intravital fluorescence microscopy using a Zeiss microscope (AxioScope; Zeiss, Germany). Leukocyte flow dynamics and leukocyte−endothelial cell interactions were studied after *in vivo* staining with rhodamine 6G (molecular weight, 476; Sigma; 2 μM/kg intravenously). Microscopic images and videos were captured by a CCD camera (AxioCam HSm, Zeiss) using 10X (N-Achroplan 0.25 N.A., Zeiss) and 20X (W N-Achroplan 0.5 N.A., Zeiss) objectives in AxioVision Rel 4.8. The blood flow was monitored in capillaries of the wound bed. At the end of each experiment, histology and immunohistochemistry assessments were performed on tissues surrounding the bacterial cellulose substrates.

Animal Histology. Tissue samples were fixed in 4% formalin and subsequently embedded in paraffin according to standard procedures. Cross sections (4 μm) were cut and stained with hematoxylin and eosin or Masson-Trichrome for histologic analysis of inflammation and tissue regeneration, respectively. The analysis was carried out by a dermatopathologist. The degree of inflammation was assessed by single-labeling with of the PAN-inflammatory marker Coronin 1[36] (1:1000, supplied by Jean Pieters, Biozentrum University of Basel, Switzerland) after antigen-retrieval in boiling citrate buffer (pH 6.0), followed by antibody incubation and detection using ABC-Vectastain (Reactolab, Servion, Switzerland). The degree of inflammation was assessed according to the following scheme: 0, no inflammation; 1, mild inflammation; 2, moderate inflammation; 3, strong inflammation.

Image Analysis. Confocal Z-stacks were projected using the maximum intensity projection function of ImageJ (National Institutes of Health, USA). Cell profiles were then manually drawn and the cell area, orientation and circularity were measured using the fit ellipse tool of ImageJ. Cell orientation was defined as the angle of the long axes of the fitted ellipse with respect to the direction of the gratings. Elongation was obtained as the ratio between short and long axes of the same ellipse. The cell density on flat and structured cellulose was measured using the "Cell Counter" tool of ImageJ (National Institutes of Health, USA). The total number of cell nuclei detected in each field of view was divided by the relative surface.

To measure the alignment of bacterial cellulose nanofibers with respect to the direction of the gratings, high magnification SEM images were loaded into ImageJ: the images were contrast-enhanced, smoothed and despeckled to reduce noise. Nanofiber orientation was then obtained using the Directionality tool of ImageJ. For both the cell and fiber orientation measurements the range of possible alignment was between 0 and 90°. Thus, a value of 0° indicates perfect alignment. Cell migration tracks were extracted using the "particle tracker" plug-in of the software Imaris (Bitplane, CH). In particular, only migratory tracks continuously detected for a minimum of 4 h were extracted and the corresponding length, average velocity, overall displacement and straightness were automatically calculated. Densitometry image analysis of collagen fiber formation were performed using Cell^P software (Olympus) on five observation windows per slide.

Lateral size or projected diameter of the fibers, surface porosity, periodicity and edge roughness were calculated from SEM images using the measurement tool of ImageJ. Surface porosity (Φ) was measured on planar images at high magnification (25000×) as the ratio of the area of pores divided by the area of the field of view. The area of the pores was calculated using the Analyze Particle tool on a binary mask obtained from the SEM image setting a signal intensity threshold. Periodicity was measured with the straight-line tool in at least 10 different locations for each field of view. Edge roughness was calculated using the standard definition of average roughness (R_a) as reported in.[43] The profile of the edge was acquired using the Freehand tool. Roughness parameters describing the topography were calculated from AFM profiles, applying standard definitions reported in.[43]

Images from intravital microscopy on the animal experiment were preprocessed with Imaris to extract skeleton images of the microvascular bed, and then analyzed using Matlab (The Math-Works, USA). Microvascular perfusion was quantified including the determination of vessel diameter, length and number of branches.

Statistical Analysis. For all reported tests three independent experiments were performed and mean values (with $n = 3$) were calculated. The results of this analysis are reported in Figures 4, 5, and 7. All quantitative measurements reported are expressed as mean values ± the standard error of the mean. Statistical significance in the reported graphs was estimated using the overlap rule for standard error of the mean bars and is indicated by * = $p < 0.05$, ** = $p < 0.01$ and *** = $p < 0.001$.[44] The total number of cells involved in each of the presented analysis is indicated in the graphs. For the descriptive analysis of

population distributions (Figures 2, 5, 6) mean values were calculated and reported with the corresponding standard error of the mean.

Conflict of Interest: The authors declare no competing financial interest.

Acknowledgment. We thank Jean Pieters for kindly providing the anti-coronin1 antibodies, Laura Bernardi and Prof. Edoardo Mazza for their support in the mechanical testing, and corresponding data interpretation and Reinier Oropesa for his support in some AFM measurements. Simone Bottan was supported by the ETH Pioneer Fellowship program. This work is part of the Zurich Heart Project.

Supporting Information Available: Summary of PDMS molds with geometrical characterization (*i.e.*, periodicity, depth and roughness). Composition of culture medium for *Acetobacter xylinum*. Representative scanning electron microscopy (SEM) of surface-structured bacterial cellulose. Representative SEM and AFM images of PDMS molds. Experimental details about mechanical tests on surface-structured and unstructured bacterial cellulose, cross sections. Experimental details about dehydration and rehydration of surface-structured bacterial cellulose. Representative SEM images of substrates featuring gelatin-coating. Results from migration experiments of HDF on bacterial cellulose substrates. Schematic illustrating the animal model. Characterization of diameter of bacterial cellulose nanofibers in different substrates. Representative phase atomic force micrographs of surface-structured bacterial cellulose substrates featuring gratings. Inverted fluorescence time-lapse of HDF migrating on a FLAT bacterial cellulose substrates. Inverted fluorescence time-lapse of HDF migrating on a surface-structured bacterial cellulose substrate (P10). This material is available free of charge *via* the Internet at http://pubs.acs.org.

REFERENCES AND NOTES

1. Langer, R.; Tirrell, D. A. Designing Materials for Biology and Medicine. *Nature* **2004**, *428*, 487–492.
2. Narayan, R. J. The Next Generation of Biomaterial Development. *Philos. Trans. R. Soc., A* **2010**, *368*, 1831–1837.
3. Bettinger, C. J.; Langer, R.; Borenstein, J. T. Engineering Substrate Topography at the Micro- and Nanoscale to Control Cell Function. *Angew. Chem., Int. Ed. Engl.* **2009**, *48*, 5406–5415.
4. Spatz, J. P.; Geiger, B. Molecular Engineering of Cellular Environments: Cell Adhesion to Nano-Digital Surfaces. *Methods Cell Biol.* **2007**, *83*, 89–111.
5. Dalby, M. J.; Gadegaard, N.; Tare, R.; Andar, A.; Riehle, M. O.; Herzyk, P.; Wilkinson, C. D.; Oreffo, R. O. The Control of Human Mesenchymal Cell Differentiation Using Nanoscale Symmetry and Disorder. *Nat. Mater.* **2007**, *6*, 997–1003.
6. Downing, T. L.; Soto, J.; Morez, C.; Houssin, T.; Fritz, A.; Yuan, F.; Chu, J.; Patel, S.; Schaffer, D. V.; Li, S. Biophysical Regulation of Epigenetic State and Cell Reprogramming. *Nat. Mater.* **2013**, *12*, 1154–1162.
7. Ferrari, A.; Cecchini, M.; Serresi, M.; Faraci, P.; Pisignano, D.; Beltram, F. Neuronal Polarity Selection by Topography-Induced Focal Adhesion Control. *Biomaterials* **2010**, *31*, 4682–4694.
8. Biela, S. A.; Su, Y.; Spatz, J. P.; Kemkemer, R. Different Sensitivity of Human Endothelial Cells, Smooth Muscle Cells and Fibroblasts to Topography in the Nano- Micro Range. *Acta Biomater.* **2009**, *5*, 2460–2466.
9. Franco, D.; Klingauf, M.; Bednarzik, M.; Cecchini, M.; Kurtcuoglu, V.; Gobrecht, J.; Poulikakos, D.; Ferrari, A. Control of Initial Endothelial Spreading by Topographic Activation of Focal Adhesion Kinase. *Soft Matter* **2011**, *7*, 7313–7324.
10. Franco, D.; Milde, F.; Klingauf, M.; Orsenigo, F.; Dejana, E.; Poulikakos, D.; Cecchini, M.; Koumoutsakos, P.; Ferrari, A.; Kurtcuoglu, V. Accelerated Endothelial Wound Healing on Microstructured Substrates Under Flow. *Biomaterials* **2013**, *34*, 1488–1497.
11. Ferrari, A.; Cecchini, M.; Dhawan, A.; Micera, S.; Tonazzini, I.; Stabile, R.; Pisignano, D.; Beltram, F. Nanotopographic Control of Neuronal Polarity. *Nano Lett.* **2011**, *11*, 505–511.
12. Marmaras, A.; Lendenmann, T.; Civenni, G.; Franco, D.; Poulikakos, D.; Kurtcuoglu, V.; Ferrari, A. Topography-Mediated Apical Guidance in Epidermal Wound Healing. *Soft Matter* **2012**, *8*, 6922–6930.
13. Potthoff, E.; Franco, D.; D'Alessandro, V.; Starck, C.; Falk, V.; Zambelli, T.; Vorholt, J. A.; Poulikakos, D.; Ferrari, A. Toward a Rational Design of Surface Textures Promoting Endothelialization. *Nano Lett.* **2014**, *14*, 1069–1079.
14. Ferrari, A.; Cecchini, M. Cells on Patterns. In *Generating Micro- and Nanopatterns on Polymeric Materials*, del Campo, A., Arzt, E., Eds.; Wiley-VCH Verlag GmbH & Co. KGaA: Weinheim, Germany, 2011; doi: 10.1002/9783527633449.
15. Dreuth, H.; Heiden, C. Thermoplastic Structuring of Thin Polymer Films. *Sens. Actuators, A* **1999**, *78*, 198–204.
16. Xia, Y.; Whitesides, G. M. Soft Lithography. *Annu. Rev. Mater. Sci.* **1998**, *28*, 153–184.
17. Cecchini, M.; Signori, F.; Pingue, P.; Bronco, S.; Ciardelli, F.; Beltram, F. High-Resolution Poly(ethylene terephthalate) (PET) Hot Embossing at Low Temperature: Thermal, Mechanical, and Optical Analysis of Nanopatterned Films. *Langmuir* **2008**, *24*, 12581–12586.
18. Janakiraman, V.; Kienitz, B. L.; Baskaran, H. Lithography Technique for Topographical Micropatterning of Collagen-Glycosaminoglycan Membranes for Tissue Engineering Applications. *J. Med. Device* **2007**, *1*, 233–237.
19. Moffa, M.; Sciancalepore, A. G.; Passione, L. G.; Pisignano, D. Combined Nano- and Micro-Scale Topographic Cues for Engineered Vascular Constructs by Electrospinning and Imprinted Micro-Patterns. *Small* **2014**, *10*, 2439–2450.
20. Helenius, G.; Backdahl, H.; Bodin, A.; Nannmark, U.; Gatenholm, P.; Risberg, B. *In Vivo* Biocompatibility of Bacterial Cellulose. *J. Biomed. Mater. Res., Part A* **2006**, *76*, 431–438.
21. Cleenwerck, I.; De Wachter, M.; Gonzalez, A.; De Vuyst, L.; De Vos, P. Differentiation of Species of the Family Acetobacteraceae by AFLP DNA Fingerprinting: *Gluconacetobacter kombuchae* is a Later Heterotypic Synonym of *Gluconacetobacter hansenii*. *Int. J. Syst. Evol. Microbiol.* **2009**, *59*, 1771–1786.
22. Klemm, D.; Heublein, B.; Fink, H. P.; Bohn, A. Cellulose: Fascinating Biopolymer and Sustainable Raw Material. *Angew. Chem., Int. Ed. Engl.* **2005**, *44*, 3358–3393.
23. Bodin, A.; Backdahl, H.; Fink, H.; Gustafsson, L.; Risberg, B.; Gatenholm, P. Influence of Cultivation Conditions on Mechanical and Morphological Properties of Bacterial Cellulose Tubes. *Biotechnol. Bioeng.* **2007**, *97*, 425–434.
24. Hu, Y.; Catchmark, J. M. Integration of Cellulases into Bacterial Cellulose: Toward Bioabsorbable Cellulose Composites. *J. Biomed. Mater. Res., Part B* **2011**, *97*, 114–123.
25. Backdahl, H.; Esguerra, M.; Delbro, D.; Risberg, B.; Gatenholm, P. Engineering Microporosity in Bacterial Cellulose Scaffolds. *J. Tissue Eng. Regener. Med.* **2008**, *2*, 320–330.
26. Ifuku, S.; Nogi, M.; Abe, K.; Handa, K.; Nakatsubo, F.; Yano, H. Surface Modification of Bacterial Cellulose Nanofibers for Property Enhancement of Optically Transparent Composites: Dependence on Acetyl-Group DS. *Biomacromolecules* **2007**, *8*, 1973–1978.
27. Fink, H.; Ahrenstedt, L.; Bodin, A.; Brumer, H.; Gatenholm, P.; Krettek, A.; Risberg, B. Bacterial Cellulose Modified with Xyloglucan Bearing the Adhesion Peptide RGD Promotes Endothelial Cell Adhesion and Metabolism—A Promising Modification for Vascular Grafts. *J. Tissue Eng. Regener. Med.* **2011**, *5*, 454–463.
28. Kargl, R.; Mohan, T.; Kostler, S.; Spirk, S.; Doliska, A.; Stana-Kleinschek, K.; Ribitsch, V. Functional Patterning of Biopolymer Thin Films Using Enzymes and Lithographic Methods. *Adv. Funct. Mater.* **2013**, *23*, 308–315.
29. Fu, L.; Zhang, J.; Yang, G. Present Status and Applications of Bacterial Cellulose-Based Materials for Skin Tissue Repair. *Carbohydr. Polym.* **2013**, *92*, 1432–1442.
30. Czaja, W. K.; Young, D. J.; Kawecki, M.; Brown, R. M., Jr. The Future Prospects of Microbial Cellulose in Biomedical Applications. *Biomacromolecules* **2007**, *8*, 1–12.

31. Sano, M. B.; Rojas, A. D.; Gatenholm, P.; Davalos, R. V. Electromagnetically Controlled Biological Assembly of Aligned Bacterial Cellulose Nanofibers. *Ann. Biomed. Eng.* **2010**, *38*, 2475–2484.
32. Albuschies, J.; Vogel, V. The Role of Filopodia in the Recognition of Nanotopographies. *Sci. Rep.* **2013**, *3*, 1658.
33. Franco, D.; Klingauf, M.; Cecchini, M.; Falk, V.; Starck, C.; Poulikakos, D.; Ferrari, A. On Cell Separation with Topographically Engineered Surfaces. *Biointerphases* **2013**, *8*, 34.
34. Milde, F.; Franco, D.; Ferrari, A.; Kurtcuoglu, V.; Poulikakos, D.; Koumoutsakos, P. Cell Image Velocimetry (CIV): Boosting the Automated Quantification of Cell Migration in Wound Healing Assays. *Integr. Biol.* **2012**, *4*, 1437–1447.
35. Lindenblatt, N.; Calcagni, M.; Contaldo, C.; Menger, M. D.; Giovanoli, P.; Vollmar, B. A New Model for Studying the Revascularization of Skin Grafts *in Vivo*: the Role of Angiogenesis. *Plast. Reconstr. Surg* **2008**, *122*, 1669–1680.
36. Pieters, J. Coronin 1 in Innate Immunity. *Subcell. Biochem.* **2008**, *48*, 116–123.
37. Recum, A. F.; Shannon, C. E.; Cannon, C. E.; Long, K. J.; Kooten, T. G.; Meyle, J. Surface Roughness, Porosity, and Texture as Modifiers of Cellular Adhesion. *Tissue Eng.* **1996**, *2*, 241–253.
38. Werner, S.; Grose, R. Regulation of Wound Healing by Growth Factors and Cytokines. *Physiol. Rev.* **2003**, *83*, 835–870.
39. Qin, D.; Xia, Y.; Whitesides, G. M. Soft Lithography for Micro- and Nanoscale Patterning. *Nat. Protoc.* **2010**, *5*, 491–502.
40. Son, H. J.; Kim, H. G.; Kim, K. K.; Kim, H. S.; Kim, Y. G.; Lee, S. J. Increased Production of Bacterial Cellulose by Acetobacter sp. V6 in Synthetic Media Under Shaking Culture Conditions. *Bioresour. Technol.* **2003**, *86*, 215–219.
41. Rohrnbauer, B.; Mazza, E. Uniaxial and Biaxial Mechanical Characterization of a Prosthetic Mesh at Different Length Scales. *J. Mech. Behav. Biomed. Mater.* **2014**, *29*, 7–19.
42. Boukamp, P.; Petrussevska, R. T.; Breitkreutz, D.; Hornung, J.; Markham, A.; Fusenig, N. E. Normal Keratinization in a Spontaneously Immortalized Aneuploid Human Keratinocyte Cell Line. *J. Cell Biol.* **1988**, *106*, 761–771.
43. Gadelmawla, E. S.; Koura, M. M.; Maksoud, T. M. A.; Elewa, I. M.; Soliman, H. H. Roughness Parameters. *J. Mater. Process. Technol.* **2002**, *123*, 133–145.
44. Cumming, G.; Fidler, F.; Vaux, D. L. Error Bars in Experimental Biology. *J. Cell Biol.* **2007**, *177*, 7–11.